Unraveling How Enzymes Can Use Bulky Residues To Drive Site-Selective C–H Activation: The Case of Mammalian Lipoxygenases Catalyzing Arachidonic Acid Oxidation

5 AUTHORS, INCLUDING:

Reynier Suardiaz
King's College London
33 PUBLICATIONS   **174** CITATIONS

SEE PROFILE

Laura Masgrau
Autonomous University of Barcelona
41 PUBLICATIONS   **727** CITATIONS

SEE PROFILE

José M Lluch
Autonomous University of Barcelona
270 PUBLICATIONS   **4,246** CITATIONS

SEE PROFILE

Angels Gonzalez-Lafont
Autonomous University of Barcelona
119 PUBLICATIONS   **1,982** CITATIONS

SEE PROFILE

Unraveling How Enzymes Can Use Bulky Residues To Drive Site-Selective C−H Activation: The Case of Mammalian Lipoxygenases Catalyzing Arachidonic Acid Oxidation

Patricia Saura,[†,‡] Reynier Suardíaz,[†,‡] Laura Masgrau,[‡] José M. Lluch,[†,‡] and Àngels González-Lafont*[,†,‡]

[†]Departament de Química and [‡]Institut de Biotecnologia i de Biomedicina (IBB), Universitat Autònoma de Barcelona, 08193 Bellaterra, Barcelona, Spain

S *Supporting Information*

ABSTRACT: The regioselective activation of C−H bonds in complex molecules containing several of them is still an exciting challenge in chemistry. However, many enzymes catalyze these processes, and much can be learned from the way they do it. For example, each mammalian lipoxygenase isoenzyme abstracts a hydrogen atom from essentially a unique carbon position. This paper presents a comprehensive study at the B3LYP(QM)/CHARMM(MM) level of the hydrogen abstraction reaction from arachidonic acid (AA) catalyzed by rabbit 15-lipoxygenase (15-rLO). Most of the products of this reaction arise from the initial hydrogen abstraction from the carbon C_{13} of AA. Nevertheless, we have shown

that 15-rLO seems able to catalyze not only the abstraction of H_{13} but also that of H_{10}. After having studied 20 of these hydrogen transfers initiated from different snapshots of an extensive MD sampling of the Michaelis complex, we have even concluded that the reaction mechanisms for both abstractions are identical (proton-coupled electron transfer processes), with transition state structures matching their geometries around the shifting hydrogen. Despite that similarity, the average potential energy barrier for the H_{13} abstractions is 4.0 kcal/mol lower than for the H_{10} abstractions, in good agreement with the experimental $C_{13}:C_{10}$ ratio of 97:3. We have found that a subtle steric hindrance by Leu597 and Ile663 is the main cause for that difference. Driving the strict regiospecificity exhibited by 15-rLO appears to be the essential function of the bulky side chains of those conserved residues, in this way making possible the vital physiological role of 15-rLO and, probably, of all the mammalian lipoxygenase isoenzymes. The understanding of how nature uses residues with the bulkiest aliphatic side chains to achieve the selective activation of C−H bonds can stimulate the design of efficient biocatalysts to that aim.

KEYWORDS: *enzyme catalysis, selective C−H activation, regiospecificity, rabbit 15-lipoxygenase-1, arachidonic acid oxidation, hydrogen abstraction, QM/MM calculations*
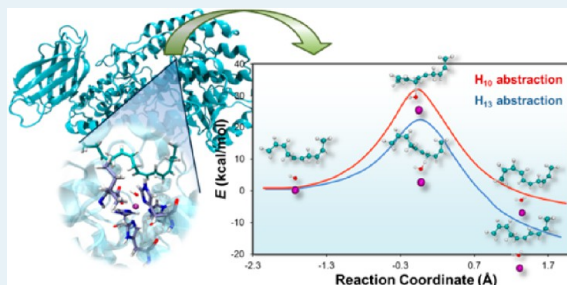
1. INTRODUCTION

Site-selective activation of C−H bonds is still a central problem in chemistry. Nevertheless, many enzymes have naturally evolved for high regiospecificity and efficiency of those reactive processes. For instance, lipoxygenases (LOs) are a family of non-heme, non-sulfur iron dioxygenases that dioxygenate the 1,4-Z,Z-pentadiene units of polyunsaturated fatty acids, producing conjugated hydroperoxy fatty acids. In mammalians the main substrate of LOs is arachidonic acid (AA), the hydroperoxidation of which initiates the biosynthesis of signaling compounds that are crucial for human health and are implicated in a number of diseases. For instance, arachidonic acid metabolites, as leukotrienes (pro-inflammatory lipid mediators) and lipoxins (anti-inflammatory lipid mediators), are involved in the inflammatory and immunity processes, which are supposed to be at the root of most illnesses.[1−4]

The different mammalian LO isoenzymes catalyze the oxygenation of AA with an exquisite regio- and stereo-specificity,[4−9] in such a way that they are named 5-, 8-, 12-,

and 15- according to their specific oxidation position on AA. The subtle similarity among the structures of these isoenzymes and among their oxidized AA products makes difficult the design of specific inhibitors. This specificity would be required due to the huge disparity (sometimes producing opposite effects) of the biological functions they have.

It is generally accepted that the rate-determining step of the overall hydroperoxidation process is the initial hydrogen atom abstraction from a bisallylic methylene group of AA by the $Fe(III)−OH^-$ moiety, yielding $Fe(II)−OH_2$ and a pentadienyl π radical. An attack of an oxygen molecule followed by a retro-hydrogen transfer to the peroxy radical finally produces the hydroperoxy product and regenerates the $Fe(III)−OH^-$ cofactor of the LO active form.[3,6]

Several hypotheses have been proposed to explain the reaction regiospecificity of the oxygen molecule addition, once a particular hydrogen atom belonging to a concrete bisallylic methylene group has been abstracted.[6,7] In particular, we have recently shown[10–13] that this regiospecificity can be explained by the oxygen-targeting hypothesis through steric-shielding residues that direct the molecular oxygen to a particular carbon atom of the corresponding pentadienyl radical in the active site of the enzyme.

Prior to that second step, the regiospecificity of the global hydroperoxidation highly depends on which is the particular pentadiene group of the fatty acid that will transfer a hydrogen atom in the first step of the process. There are three bisallylic methylene groups in AA, each containing two C−H bonds. It is assumed that the nearness of the bisallylic methylene carbon atoms to the Fe(III)−OH⁻ moiety highly determines the hydrogen atom to be abstracted. For a given fatty acid, that closeness would greatly depend on the depth and width of the substrate binding pocket and the head/tail orientation of the incoming fatty acid (carboxyl or tail end first).[4,5] This way, each LO isoenzyme would abstract a hydrogen atom from essentially a unique position.

Reticulocyte-type 15-LO-1 has been one of the most studied mammalian LOs in recent years. The X-ray structure of human 15-LO-1 (15-hLO) has still to be reported, but the corresponding crystallographic structure for rabbit 15-LO-1 (15-rLO) was the first one resolved[14,15] for a mammalian LO (PDB code 2P0M). It has to be noted that 15-rLO has approximately 80% sequence identity[16] with 15-hLO. Most of the products generated by the reaction of 15-hLO with AA come from the initial hydrogen abstraction from the carbon C_{13} (with, for instance, a C_{13}:C_{10} ratio of 10:1[17] or 89:11[18]). The same holds for 15-rLO, with a C_{13}:C_{10} ratio of 97:3.[19] Interestingly, a dramatic inversion in the regiospecificity of the reaction of 15-hLO with AA occurs when the methylene group of AA at position 13 is dideuterated, with the products derived from hydrogen abstraction from C_{10} being now predominant by a ratio C_{13}:C_{10} of 25:75. In addition, it has been experimentally determined that the H/D kinetic isotope effects (KIEs) for the hydrogen abstraction steps from C_{13} and C_{10} in 15-hLO turn out to be comparable ($^Dk_{cat} = 11.6 \pm 2.0$ and $^Dk_{cat} = 8.5 \pm 4.0$, respectively). The corresponding $^Dk_{cat}/K_M$ values are also comparable for the two carbon centers. From these results, Holman and co-workers[18,20] have suggested that the hydrogen abstraction at these two structurally different positions (C_{13} and C_{10}) follows a comparable mechanism with, probably, very similar transition state structures. This assumption was found to be quite unexpected by those authors because 15-hLO would be able to spatially accommodate these two disparate carbon positions in a similar way, despite being a highly regiospecific enzyme. On the other hand, we have recently[21] combined protein−ligand docking, molecular dynamics simulations, and in silico mutagenesis to study the binding modes of AA in the active site of 15-rLO. Our simulations gave similar average values for the C_{13}/H_{13}−OH⁻−Fe(III) and C_{10}/H_{10}−OH⁻−Fe(III) distances, in such a way that those carbon atoms are not really in structurally different locations in a great number of configurations of the 15-rLO:AA Michaelis complex. Even more, the distances corresponding to C_{10} tend to be somewhat smaller than the ones in the case of C_{13}, and so, not only do both hydrogen abstractions seem to be possible, but hydrogen abstraction from C_{10} could be guessed as the most favorable, contrarily to the experimental evidence.

Thus, how does 15-hLO (and 15-rLO) manage to achieve such an exquisite regiospecificity?

At this point, it is worth noting that, in general terms, the first step of the hydroperoxidation of AA can be considered as a carbon−hydrogen bond activation[22] where several carbon atoms are candidates to be functionalized, but only one of them will be essentially affected. This fact is especially relevant when it is taken into account that targeting a specific C−H bond is very difficult if various practically equivalent C−H bonds exist in the molecule.[23–25] In this sense, lipoxygenases are able to catalyze the activation of quite unreactive C−H bonds, and, very interestingly, with a huge selectivity.

In this paper our goal is to get a deep insight on the mechanism of the hydrogen abstraction reaction from AA catalyzed by 15-rLO, which can serve as a model of 15-hLO. We will put special emphasis on shedding light on the subtle factors that govern the strict regiospecificity of this first step of the hydroperoxidation of AA despite the fact that, in principle, the hydrogen abstractions from both C_{13} and C_{10} would seem to be plausible. To this aim, we have carried out quantum mechanics/molecular mechanics (QM/MM) calculations on the entire solvated 15-rLO:AA complex, employing the density functional theory (DFT) to treat the QM region to obtain a reliable enough description of the evolution of the electronic structure of the system along the reaction and of the chemical properties depending on it.

2. COMPUTATIONAL METHODS

In the present work all QM/MM calculations have been performed with the modular program package ChemShell,[26] using TURBOMOLE[27] for all of the DFT calculations. The MM calculations were carried out by the DL_POLY[28] module in ChemShell, using the CHARMM22[29,30] and CHARMM27[31,32] (for the lipid moiety included in the MM region) force fields. An electronic embedding scheme[33] has been adopted in all calculations, and a hydrogen link atoms scheme has been employed to treat the QM/MM boundary using the charge shift model. No cutoffs were introduced for the nonbonding MM and QM/MM interactions.[34]

QM/MM optimizations were carried out employing the limited-memory Broyden−Fletcher−Goldfard−Shanno (L-BFGS) algorithm[35,36] in the case of energy minimizations, and the microiterative optimizer, combining both the partitioned rational function optimizer (P-RFO)[37,38] and the L-BFGS, was used during the transition state searches. All of these algorithms are implemented in the HDLCopt (Hybrid Delocalized Internal Coordinate Scheme)[39] ChemShell module. We have taken the natural population analysis (NPA)[40] atomic populations evaluated from the spin density as implemented in TURBOMOLE. The VMD program[41] has been used to generate the pictures of molecules.

In all calculations the QM subsystem has been described by the B3LYP hybrid functional, and the 6-31G(d) Pople basis set[42] has been used for all atoms except for Fe, which was described by the LANL2DZ basis set.[43] The QM/MM partition is shown in Figure 1. The QM region includes 74 atoms (link atoms not included): 24 atoms of lipid substrate, 11 atoms of each of the 4 His residues in the Fe coordination sphere (His361, His366, His541, and His545), 3 atoms of the terminal Ile663 in the coordination sphere, and the Fe(III)−OH⁻ cofactor, able to accept the hydrogen from AA. Seven link atoms were used, five along the bonds Cα−QM atom of the five residues in the Fe coordination sphere and two bonded to
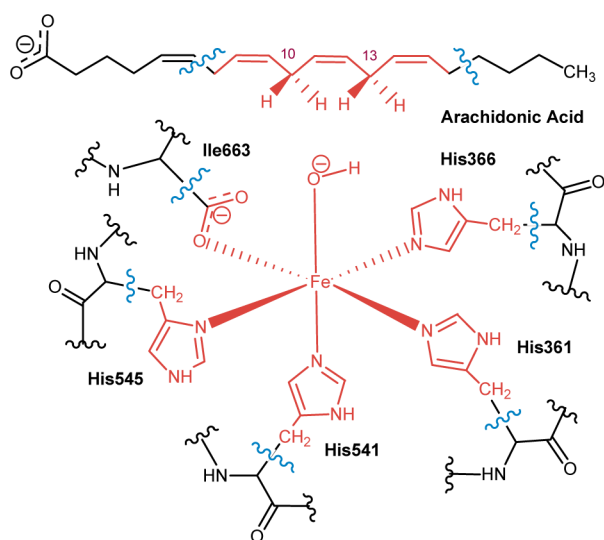
Figure 1. QM/MM partition. QM atoms are depicted in red. The boundary between QM and MM regions is indicated by blue wavy lines. This scheme represents the reactants of the investigated reaction.

the aliphatic carbons of the lipid substrate (placed between C_6–C_7 and C_{16}–C_{17}).

The geometries studied in the present paper have been taken from a previous work, in which a series of long classical molecular dynamics (MD) trajectories under periodic boundary conditions of the AA:15-rLO Michaelis complexes were performed. Considering the snapshots of these trajectories, a selection criterion has been applied to finally choose the reactive structures studied in this work.

3. RESULTS AND DISCUSSION

3.1. Selection of Starting Geometries. As mentioned above, a selection criterion has been applied to the structures of previously[21] generated long classical MD trajectories of the AA:15-rLO Michaelis complexes to select those structures having characteristics that have been considered adequate to initiate the reactive processes. This criterion is based on the initial distance between the hydrogen atom that would be abstracted, pro-S H_{13} and/or pro-S H_{10} (hereafter referred only as H_{13} and H_{10}, respectively), and the oxygen atom of the hydrogen acceptor, that is, the oxygen of the Fe(III)–OH^- cofactor. This distance has been established to be ≤3.0 Å for

the reaction to take place. Furthermore, the distance from the corresponding carbon atom, C_{13} or C_{10}, to that oxygen atom had to be greater than the distance from H_{13} and H_{10}, respectively, thus ensuring that the corresponding C−H bond is properly oriented for hydrogen abstraction.

Following application of this selection criterion, a set of structures was filtered from the rest that do not fulfill the required characteristics. The selection process was repeated three times: applying the selection criterion only to H_{13}, only to H_{10}, or to both at once; therefore, we have studied three types of structures. There are significantly more structures with the H_{10} close to the Fe(III)—OH^- cofactor than with the H_{13}, as was already reported in our previous mentioned work. From such filtered structures, nine suitable for H_{13} abstraction, six suitable for H_{10} abstraction, and two suitable for both reactive processes were chosen.

For the selected geometries, all of the water molecules outside a 15 Å radius volume centered on the AA molecule have been removed. All residues and water molecules included in a 15 Å radius sphere centered on the C_{11} of the AA molecule, along with the complete AA, were included in the active region during the optimization processes and allowed to move freely, whereas the remaining atoms were kept frozen.

Finally, the geometries of those 17 structures were optimized to obtain the reactive minima, the main characteristics of which are shown in Tables 1 and 2. Those reactive minima have been used as starting points to build the QM/MM potential energy profiles for the hydrogen abstractions of H_{13} (structures I−IX), H_{10} (structures XII−XVII), or any of them (structures X and XI) of the AA by the oxygen atom of the Fe(III)−OH^- cofactor. It can be seen that the set of these reactive minima covers a wide region of the configurational space. For instance, the dispersion of geometries is such that the distance from the hydrogen atom to be transferred to the acceptor oxygen atom ranges from 2.47 to 3.78 Å for structures I−IX (H_{13}) and from 2.67 to 3.16 Å for structures XII−XVII (H_{10}).

The QM part used (described above) was the same for all investigated structures. The remaining atoms comprise the MM part of the system. Table S1 shows the total number of atoms of each of the structures in question, indicating the number of active atoms. These numbers differ for the different structures because the number of selected water molecules may vary. A complete view of one of the AA:15-rLO Michaelis complexes we have studied is pictured in Figure 2.

Table 1. Main Geometric Parameters of Reactants and TSs of H_{13} Abstraction[a]

structure	$d(C−H)_R$	$d(O−H)_R$	$d(C−O)_R$	$\angle(C−H−O)_R$	$\angle(H−O−H)_R$	$d(C−H)_{TS}$	$d(O−H)_{TS}$	$d(C−O)_{TS}$	$\angle(C−H−O)_{TS}$	$\angle(H−O−H)_{TS}$
I	1.10	2.64	3.64	149.0	78.9	1.34	1.33	2.65	167.2	98.3
II	1.11	3.64	4.02	102.0	57.3	1.31	1.36	2.65	166.9	99.2
III	1.10	2.96	3.80	133.5	70.2	1.27	1.40	2.66	171.4	97.4
IV	1.10	3.27	3.92	118.7	76.2	1.31	1.35	2.65	173.9	99.8
V	1.11	3.78	4.09	98.2	50.5	1.32	1.33	2.64	167.5	95.9
VI	1.10	2.47	3.50	155.6	87.4	1.35	1.31	2.64	166.6	100.4
VII	1.10	2.75	3.72	146.6	83.4	1.34	1.33	2.65	165.8	99.2
VIII	1.10	3.17	3.91	124.9	116.2	1.31	1.33	2.62	165.2	99.6
IX	1.10	3.09	3.85	126.2	113.6	1.30	1.36	2.63	163.2	99.7
X	1.09	4.02	4.94	142.9	119.9	1.32	1.35	2.66	172.6	105.1
XI	1.10	3.83	4.24	104.5	99.5	1.30	1.34	2.62	165.7	99.9

[a]Distances are given in Å and angles in degrees. H stands for the hydrogen atom to be transferred, C is the carbon atom to which H is attached, and O is the acceptor oxygen atom.

Table 2. Main Geometric Parameters of Reactants and TSs of H$_{10}$ Abstraction[a]

structure	$d(C-H)_R$	$d(O-H)_R$	$d(C-O)_R$	$\angle(C-H-O)_R$	$\angle(H-O-H)_R$	$d(C-H)_{TS}$	$d(O-H)_{TS}$	$d(C-O)_{TS}$	$\angle(C-H-O)_{TS}$	$\angle(H-O-H)_{TS}$
XII	1.10	2.86	3.78	141.0	78.0	1.34	1.33	2.67	175.5	99.5
XIII	1.10	2.71	3.76	161.7	99.8	1.34	1.30	2.64	174.8	101.7
XIV	1.10	3.08	3.94	135.4	68.7	1.31	1.36	2.67	175.0	97.4
XV	1.10	2.67	3.73	161.6	94.0	1.34	1.30	2.64	172.0	102.5
XVI	1.10	3.16	3.86	122.5	59.9	1.34	1.33	2.65	171.0	97.4
XVII	1.10	3.14	3.82	121.3	34.5	1.33	1.30	2.63	170.5	90.3
I	1.10	5.83	5.85	85.7	55.9	1.30	1.39	2.69	173.8	91.0
X	1.10	3.74	4.15	104.5	68.6	1.32	1.37	2.69	175.5	99.7
XI	1.10	3.75	4.08	99.7	37.9	1.28	1.38	2.66	174.6	93.4

[a]Distances are given in Å and angles in degrees. H stands for the hydrogen atom to be transferred, C is the carbon atom to which H is attached, and O is the acceptor oxygen atom.
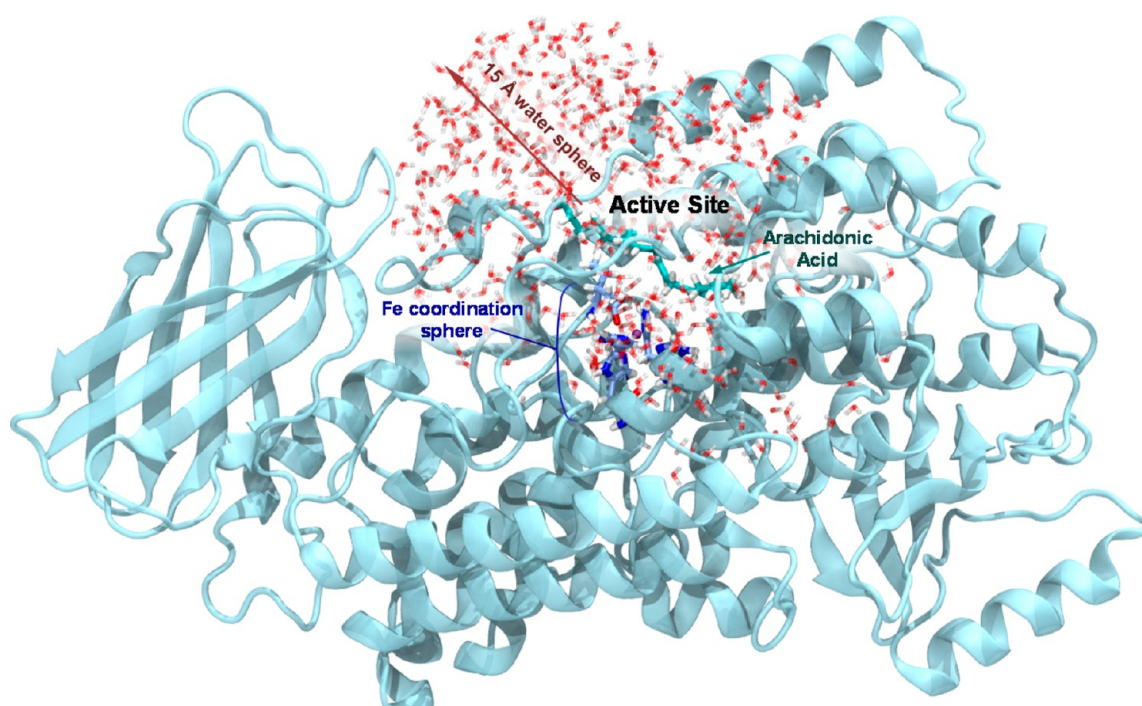

Figure 2. Complete view of the AA:15-rLO Michaelis complex. In particular, this image corresponds to structure I. Atoms of substrate (arachidonic acid), coordination sphere, and water molecules are highlighted by using the licorice drawing method.

3.2. Potential Energy Profiles and Reaction Mechanism.

This section describes the procedure used for the study of the reactivity of all structures (I–XVII) and the corresponding results. For the sake of brevity, we essentially focus on one case corresponding to a suitable structure for H$_{13}$ abstraction (structure I), one appropriate structure for H$_{10}$ abstraction (structure XII), and a suitable third one for both reactive processes (structure XI). Panels a and b of Figure 3 show the active sites of structures I and XII, respectively.

First, the optimized geometry corresponding to the reactive structure has been used as a starting point to build the potential energy profile along the reaction coordinate. The reaction coordinate, z, is defined as the difference between the distance of the breaking bond (C$_{13}$–H$_{13}$ or C$_{10}$–H$_{10}$ for H$_{13}$ or H$_{10}$ abstractions, respectively) and the forming bond (H$_{13}$–O or H$_{10}$–O, respectively). To construct the potential energy profile, a series of optimizations of the mobile part of the system have been performed in the presence of harmonic restrictions on the reaction coordinate as

$$V = \frac{k}{2}(z - z^0)^2 \qquad (1)$$

where k is the force constant, which has been set equal to 3.0 hartree/Bohr^2, and z^0 is the reference value for the reaction coordinate z at each energy minimization calculation, which increases with a step size of 0.1 Å.

From the maximum energy point of the potential energy profile, the transition state structure was directly located using, as mentioned above, a microiterative optimization procedure. A small core that contains six atoms (C$_{13}$, pro-S H$_{13}$, pro-R H$_{13}$, and Fe–OH$^-$ cofactor) has been employed, and a transition state structure search has been performed with the P-RFO algorithm, which uses the Hessian matrix explicitly, whereas the rest of the mobile part of the system is minimized by the L-BFGS method. A saddle point type structure is obtained, and the frequency calculations show that this structure has a single imaginary frequency (Table 3) and the normal mode corresponds to the investigated reaction. Table 1 shows that the transition state has very similar distances between H$_{13}$ and its donor atom (C$_{13}$–H$_{13}$) and between H$_{13}$ and its acceptor
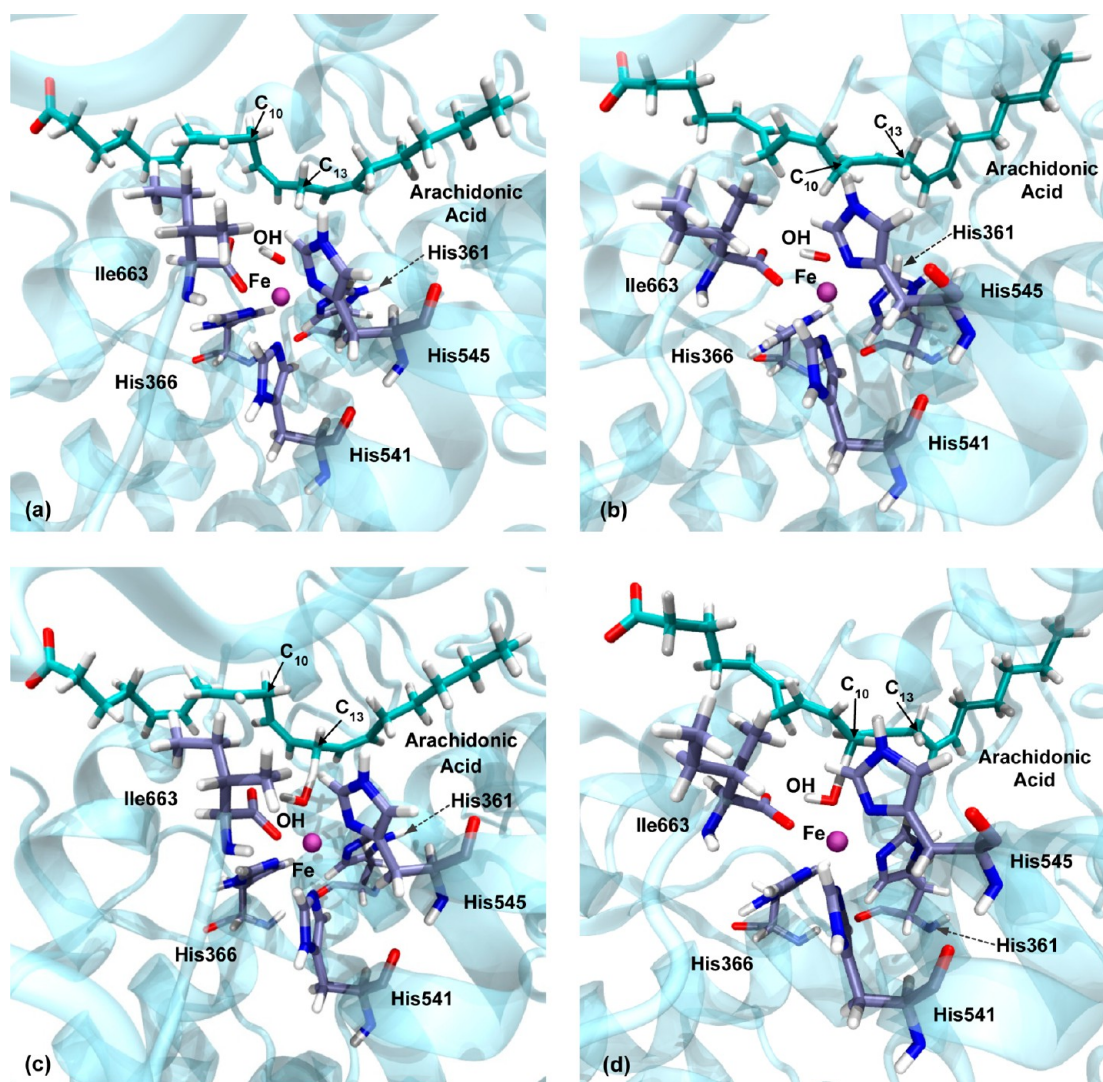
Figure 3. Representation of the 15-rLO active site, showing the substrate (arachidonic acid) and the Fe coordination sphere (all of these atoms are highlighted by using licorice drawing methods) at the following stationary points: (a) reactant, structure I; (b) reactant, structure XII; (c) TS, structure I; (d) TS, structure XII.

atom $(O-H_{13})$ (1.34 and 1.33 Å, respectively) and, therefore, as for the H transfer, it is highly symmetrical. To reach the transition state, the donor and acceptor atoms need to approach each other from 3.64 to 2.65 Å, with the $C_{13}-H_{13}-O$ angle becoming fairly linear (167.2°), and the angle $H_{13}-O-H$ already adopting nearly the value corresponding to the water molecule finally formed (see Figure 3c). In all of the studied structures a transition state structure was found following this procedure (for H_{10} abstraction the core atoms are C_{10}, pro-S H_{10}, pro-R H_{10}, and the $Fe-OH^-$ cofactor).

For the H_{13} abstraction in structure I, the potential energy barrier turns out to be 21.6 kcal/mol and the reaction is exoergic by 12.9 kcal/mol (see Table 3). The reactant is located at $z = -1.54$ Å, the transition state (TS) at $z = 0.01$ Å, and the product at $z = 2.33$ Å. The NPA atomic populations evaluated from the spin density, which indicate the atomic excess of α spin, along the potential energy profile have been calculated, as indicated under Computational Methods. The evolution of the spin densities on C_{11}, C_{12}, C_{13}, C_{14}, and C_{15} of the pentadienyl system, H_{13}, and the Fe atom of the active site is shown in Figure 4a. The spin density on Fe decreases from 4.1 to 3.7 au, as corresponds to the transition of a Fe(III) sextet

configuration to a Fe(II) quintet configuration. As H_{13} is being transferred, a growing spin density appears on C_{13}, which is becoming delocalized over C_{13}, C_{11}, and C_{15} along the reaction, going from 0 au to around 0.4 au on each one of these atoms. The latter two, therefore, will be the hit points of molecular oxygen during the next step of the hydroperoxidation process. The spin densities on C_{12} and C_{14} go from 0 to −0.15 au. In turn, the spin density on H_{13} remains virtually zero during the process, suggesting that this atom is rather a proton than a hydrogen atom with its electron. The representation of the spin density isosurfaces, as shown in Figure 5, provides a good pictorial view of those changes. On the other hand, the NPA net charges on the H_{13} atom during the reaction (Figure 4b) are positive and go from nearly 0.3 to 0.5 au, confirming that this atom is in fact a proton. All of these analyses of the evolution of the electronic structure along the transfer show that the hydrogen abstraction is actually a proton coupled electron transfer (PCET) process,[44−47] in which the electron and proton are transferred in a concerted way to different acceptors: the proton is transferred to the OH^- group oxygen to produce water, whereas the electron is transferred from the $C_{11}-C_{15}$ pentadiene group of AA to the Fe(III) to give Fe(II).

Table 3. Potential Energy Barriers, $\Delta E^{\ddagger}_{\text{Total}}$, Reaction Energies, $\Delta E_{\text{R,Total}}$, and TS Imaginary Frequencies, $\bar{\nu}_{\text{TS}}$, of H_{13} and H_{10} Abstractions

structure	abstraction	$\Delta E^{\ddagger}_{\text{(QM,MM)}}$ [a] (kcal/mol)	$\Delta E^{\ddagger}_{\text{(MM,QM)}}$ [b] (kcal/mol)	$\Delta E^{\ddagger}_{\text{Total}}$ (kcal/mol)	$\Delta E_{\text{R,Total}}$ (kcal/mol)	$\bar{\nu}_{\text{TS}}$ (cm^{-1})
I	H_{13}	21.5	0.1	21.6	−12.9	1773 i
II	H_{13}	18.2	4.1	22.3	−16.5	1682 i
III	H_{13}	20.3	−0.7	19.6	−10.2	1312 i
IV	H_{13}	22.5	−0.3	22.2	−11.8	1648 i
V	H_{13}	22.8	1.9	24.7	−16.5	1771 i
VI	H_{13}	21.8	−3.2	18.6	−15.0	1885 i
VII	H_{13}	22.4	1.0	23.4	−14.6	1808 i
VIII	H_{13}	13.7	5.2	18.9	−21.7	1708 i
IX	H_{13}	17.5	3.1	20.6	−15.1	1627 i
X	H_{13}	24.2	6.2	30.4	−10.2	1697 i
XI	H_{13}	20.6	1.9	22.5	−17.2	1642 i
XII	H_{10}	22.4	1.7	24.1	−11.8	1812 i
XIII	H_{10}	22.0	1.6	23.6	−7.6	1774 i
XIV	H_{10}	17.4	5.3	22.7	−9.5	1639 i
XV	H_{10}	18.6	5.7	24.3	−12.5	1803 i
XVI	H_{10}	26.0	−0.2	25.8	−16.0	1848 i
XVII	H_{10}	33.2	−1.8	31.4	−9.3	1888 i
I	H_{10}	32.8	7.8	40.6	−8.8	1528 i
X	H_{10}	20.2	8.9	29.1	−9.1	1681 i
XI	H_{10}	22.2	8.7	30.9	−11.5	1437 i

[a]Contribution to the barrier of the QM energy plus the electrostatic interaction between the QM and MM subsystems. [b]Contribution to the barrier of the MM energy and the bonded and van der Waals interactions between the QM and MM subsystems.
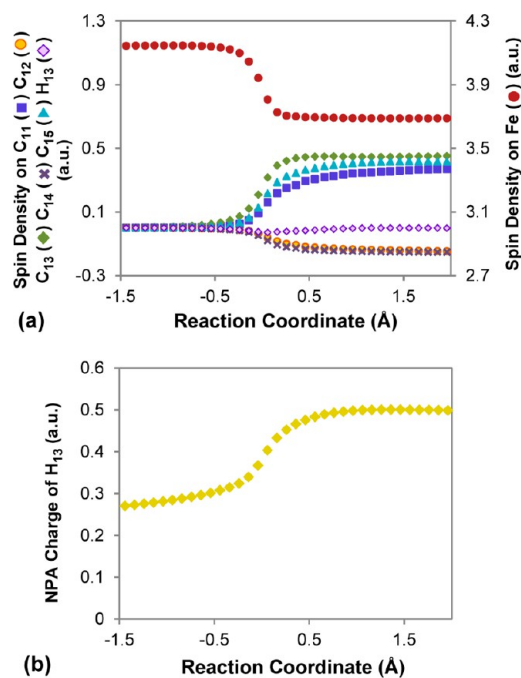
Figure 4. (a) Spin densities on atoms C_{11}, C_{12}, C_{13}, C_{14}, C_{15}, H_{13}, and Fe and (b) NPA charges on H_{13}, during H_{13} abstraction on structure I.

As for the evolution of the electronic structure and the geometry of the corresponding transition state structure, all of the H_{13} abstractions we have analyzed (for structures I−XI) behave as the one in structure I. Very interestingly, the geometries of all the transition state structures around the shifting H_{13} are very similar (see Table 1), despite the existence of a wide dispersion of structures corresponding to reactants, as mentioned above. It has to be emphasized that, within the set of the 11 transition state structures, the differences between the larger and the smaller values of the C_{13}−H_{13}, O−H_{13}, and C_{13}−

O distances and the C_{13}−H_{13}−O and H_{13}−O−H angles are as small as 0.08, 0.09, and 0.04 Å and 10.7° and 9.2°, respectively. These values turn out to be extraordinarily lower than the corresponding values within the set of the 11 structures I−XI, which are 0.02, 1.55, and 1.44 Å and 57.4° and 69.4°, respectively. On the other hand, what actually makes a difference among the H_{13} abstractions is the height of the potential energy barriers, which range from 18.6 kcal/mol (structure VI) to 30.4 kcal/mol (structure X), and the reaction energies, ranging from −21.7 kcal/mol (structure VIII) to −10.2 kcal/mol (structures III and X). These results suggest that the differences observed in the potential energy barriers are primarily due to the differences among the structures of the reactive minima rather than the transition state ones.

Following the same procedure described above, the analysis of the H_{10} abstraction on structure XII will be now presented. From the geometrical point of view the scenario is roughly identical to the one for abstraction of H_{13} on structure I. The transition state structure (see Table 2 and Figure 3d) has very similar distances between H_{10} and its donor atom (C_{10}−H_{10}) and between H_{10} and its acceptor atom (O−H_{10}) (1.34 and 1.33 Å, respectively), and to reach the transition state the donor and acceptor atoms need to approach each other by a bit more than 1 Å (from 3.78 to 2.67 Å), with the C_{10}−H_{10}−O angle becoming almost linear, with a value of 175.5°, and the angle H_{10}−O−H already adopting nearly the value corresponding to the water molecule finally formed (see Figure 3d). The potential energy barrier is 24.1 kcal/mol (>2 kcal/mol higher than for abstraction of H_{13} on structure I), and the reaction is exoergic by 11.8 kcal/mol. The reactant is located at z = 1.76 Å, the TS at z = 0.01 Å, and the product at z = 2.24 Å. On the other hand, changing the corresponding atoms, the evolution of the NPA atomic populations evaluated from the spin density matches the H_{13} case. Initially, an α spin density appears on C_{10} and delocalizes over C_{10}, C_8, and C_{12} as the H_{10} transfer progresses. The latter two carbon atoms will be the hit points of
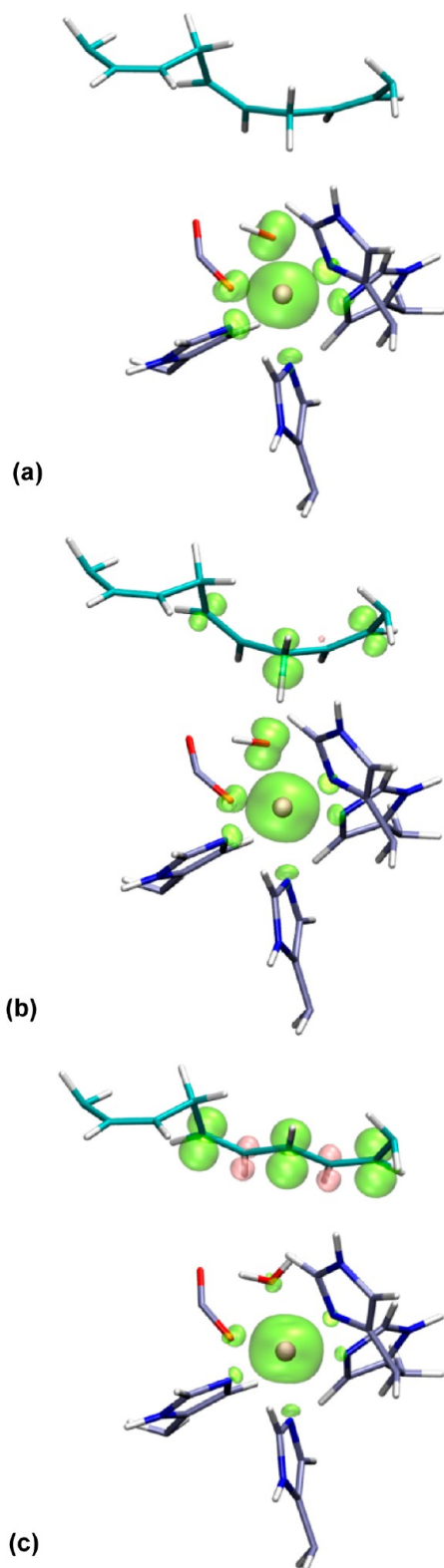
Figure 5. Representation of spin density surfaces. Green surface corresponds to α spin density, and pink surface corresponds to β spin density. Only QM atoms are shown. These pictures correspond to structure I: (a) reactant; (b) TS; (c) product of H_{13} abstraction.

the molecular oxygen in the following step of the mechanism. The H_{10} atom behaves as a proton: its spin density remains virtually zero, and its NPA net charge is increasingly positive during the transfer. Therefore, the H_{10} abstraction is also a

PCET process, with the electron being transferred from the C_8−C_{12} pentadiene group of AA (see Figure 6).
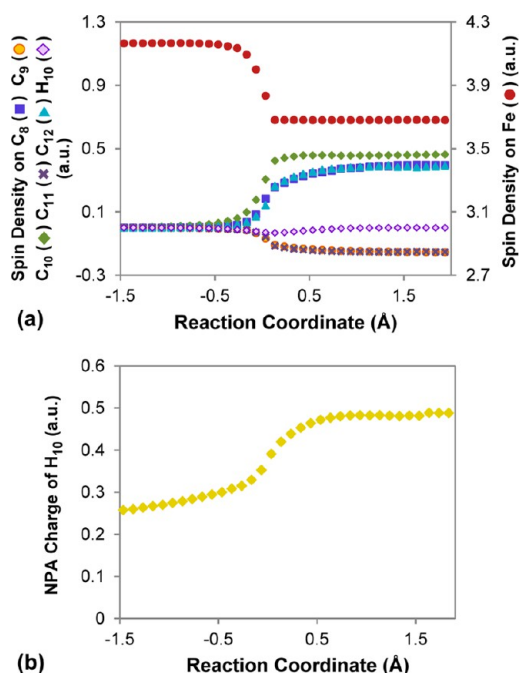

Figure 6. (a) Spin densities on atoms C_8, C_9, C_{10}, C_{11}, C_{12}, H_{10}, and Fe and (b) NPA charges on H_{10}, during H_{10} abstraction on structure XII.

Analyzing the rest of the H_{10} abstractions, we see that this process is feasible provided that the initial conditions in the reactive complexes are appropriate. Again, the initial noticeable dispersion in the configurational space within the set of the eight structures X−XVII, measured as the differences between the largest and the smallest values of the C_{10}−H_{10}, O−H_{10}, and C_{10}−O distances and the C_{10}−H_{10}−O and H_{10}−O−H angles (0.00, 1.08, and 0.42 Å and 62.0° and 65.3°, respectively), is highly reduced within the set of the eight transition state structures (see Table 2), for which geometries around the jumping H_{10} match quite well one another (the corresponding values of those differences are 0.06, 0.08, and 0.06 Å and 5.0° and 12.2°, respectively). Again, the important difference among the transition state structures lies on the height of the potential energy barriers (see Table 3), which ranges from 22.7 kcal/mol (structure XIV) to 31.4 kcal/mol (structure XVII), an interval of energies somewhat higher than the one for the H_{13} abstraction. Likewise, there exists certain dispersion on the values of reaction energies, ranging from −16 kcal/mol (structure XVI) to −7.6 kcal/mol (structure XIII), an interval somewhat less exoergic than in the case of the H_{13} abstractions. In Tables 2 and 3 we have also included the results corresponding to the H_{10} abstraction in structure I, which, as previously mentioned, is suitable for an H_{13} abstraction but not for an H_{10} abstraction because the initial O−H_{10} and C_{10}−O distances are as large as 5.83 and 5.85 Å, respectively. Very interestingly, even in this case the transition state structure converges to exactly the same zone of the configurational space as the other H_{10} abstractions, although, indeed, the potential energy barrier appears completely out of range (40.6 kcal/mol).

At this point we can compare the H_{13} with the H_{10} abstractions. It is evident that only those reactive complexes

that have a methylene hydrogen of AA close to the acceptor oxygen atom of the Fe(III)−OH⁻ cofactor are able to allow a thermally feasible hydrogen transfer. In the case of 15-rLO, only the reactive complexes with H_{13} or H_{10} near the acceptor oxygen atom are thermally accessible. As a consequence, only the H_{13} or H_{10} abstraction is possible. Our results have shown that, starting from the convenient reactive structures, the reaction mechanisms for both H_{13} and H_{10} abstractions are identical, with transition state structures that involve matching geometries around the shifting hydrogen. Therefore, we have confirmed the suggestion by Holman and co-workers[18,20] about the similarity of the mechanisms and transition states for both abstractions, a fact that explains the comparable experimental $^{D}k_{cat}$ and $^{D}k_{cat}/K_{M}$ values for the two carbon centers in 15-hLO.

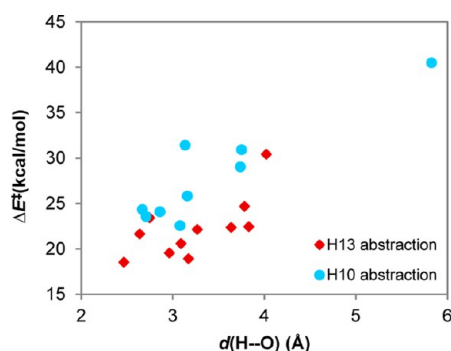The main difference between the H_{13} and H_{10} abstractions lies in the respective potential energy barriers. Figure 7 displays

Figure 7. Potential energy barriers versus initial H−O distances for H_{13} and H_{10} abstractions.

the potential energy barriers for the 20 hydrogen abstractions studied in this work as a function of the corresponding H−O (H_{13}−O or H_{10}−O) distance in each reactive structure. First, we can see that in some way the barriers tend to increase as the H−O distance becomes larger, although it is not possible to establish a precise correlation between the values of the potential energy barriers and the initial H−O distances. It is clear that, the transition state structures being equivalent, the barrier height depends on the geometry of the reactive structures, although many additional parameters define it. Note the huge value of 40 kcal/mol for the H_{10} abstraction in structure I, which is not suitable for that abstraction (the O−H_{10} distance is 5.83 Å) but for the H_{13} abstraction (the O−H_{13} distance is 2.64 Å). This difference in the energy barriers is why most of the products generated by the reaction of 15-LO with AA come from the hydrogen abstraction from C_{13}, despite the fact that both H_{13} and H_{10} are spatially accessible for the abstraction. Other plots displaying the potential energy barriers for the 20 hydrogen abstractions versus different geometrical parameters at reactants and at the transition states have been included in the Supporting Information (Figure S1) looking for any correlation between geometry and barrier height.

Now the point is why apparently H_{13}/H_{10} identical abstraction mechanisms and very similar transition state structures occur with somewhat different potential energy barriers, in this way preserving the exquisite regiospecificity of 15-rLO. To make a more detailed comparison between the potential energy barriers, the total QM/MM energy has been decomposed as

$$E_{Total} = E_{(QM,MM)} + E_{(MM,QM)} \qquad (2)$$

where $E_{(QM,MM)}$ is the sum of the QM energy and the electrostatic interaction between the QM and MM subsystems and $E_{(MM,QM)}$ is the sum of the MM energy and the bonded and van der Waals interactions between the QM and MM subsystems. Results are listed in Table 3. We can highlight two facts. First, almost identical values of the total potential energy barriers decompose in a different way. For instance, for the H_{13} abstraction 22.3 kcal/mol (structure II), 22.2 kcal/mol (structure IV), and 22.5 kcal/mol (structure XI) decompose into 18.2, 22.5, and 20.6 kcal/mol, respectively, for the $E_{(QM,MM)}$ component and into 4.1, −0.3, and 1.9 kcal/mol, respectively, for the $E_{(MM,QM)}$ component. This is a consequence of the diversity of initial structures that have to evolve in a different manner to reach very similar transition state structures. Second, in a few cases the $E_{(QM,MM)}$ component is <20 kcal/mol, but then the $E_{(MM,QM)}$ component turns out to be quite large. This is especially true for the H_{10} abstractions. This indicates that, in some initial structures, the better the QM part is ready to react, the worse prepared is the corresponding MM part (either itself or due to the nonelectrostatic interaction with the QM part).

To get a deeper insight on the differences between the H_{13}/H_{10} abstractions, we will focus now on structure XI (see Figure 8), where the C_{13}−O and C_{10}−O distances (3.83 and 3.75 Å,
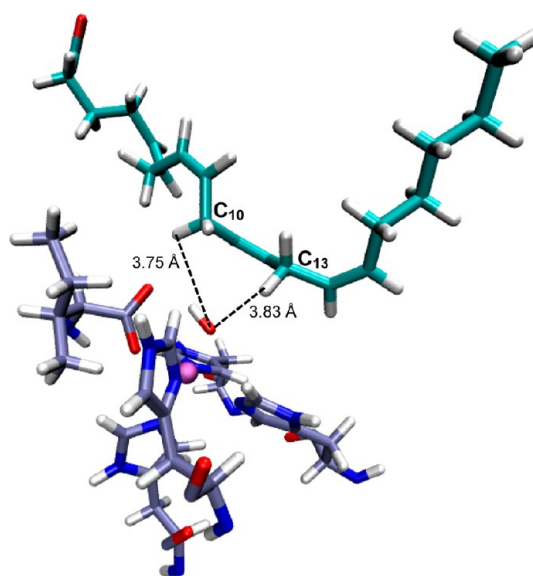

Figure 8. Reactant of structure XI. AA and Fe coordination sphere are shown. H_{13}—O and H_{10}—O distances are indicated.

respectively) are practically equal, which seems ready to allow any of the two possible hydrogen transfers. The existence of this structure shows that a highly regiospecific enzyme such as 15-rLO (or 15-hLO) is able to spatially accommodate the two carbon positions (C_{13} and C_{10}), even at once, in a similar way with respect to the acceptor Fe(III)−OH⁻ moiety. However, the potential energy barrier for the H_{10} abstraction turns out to be >8 kcal/mol higher than the corresponding to the H_{13} abstraction (see Table 3), the difference mostly arising from the $E_{(MM,QM)}$ component (6.8 kcal/mol). Likewise, the H_{13} abstraction is 5.7 kcal/mol more exoergic than the H_{10} abstraction.

As the H_{13} hydrogen transfer progresses in a given reactive structure, C_{13} tends to an sp^2 hybridization and the moiety corresponding to the nascent AA-pentadienyl radical ap-
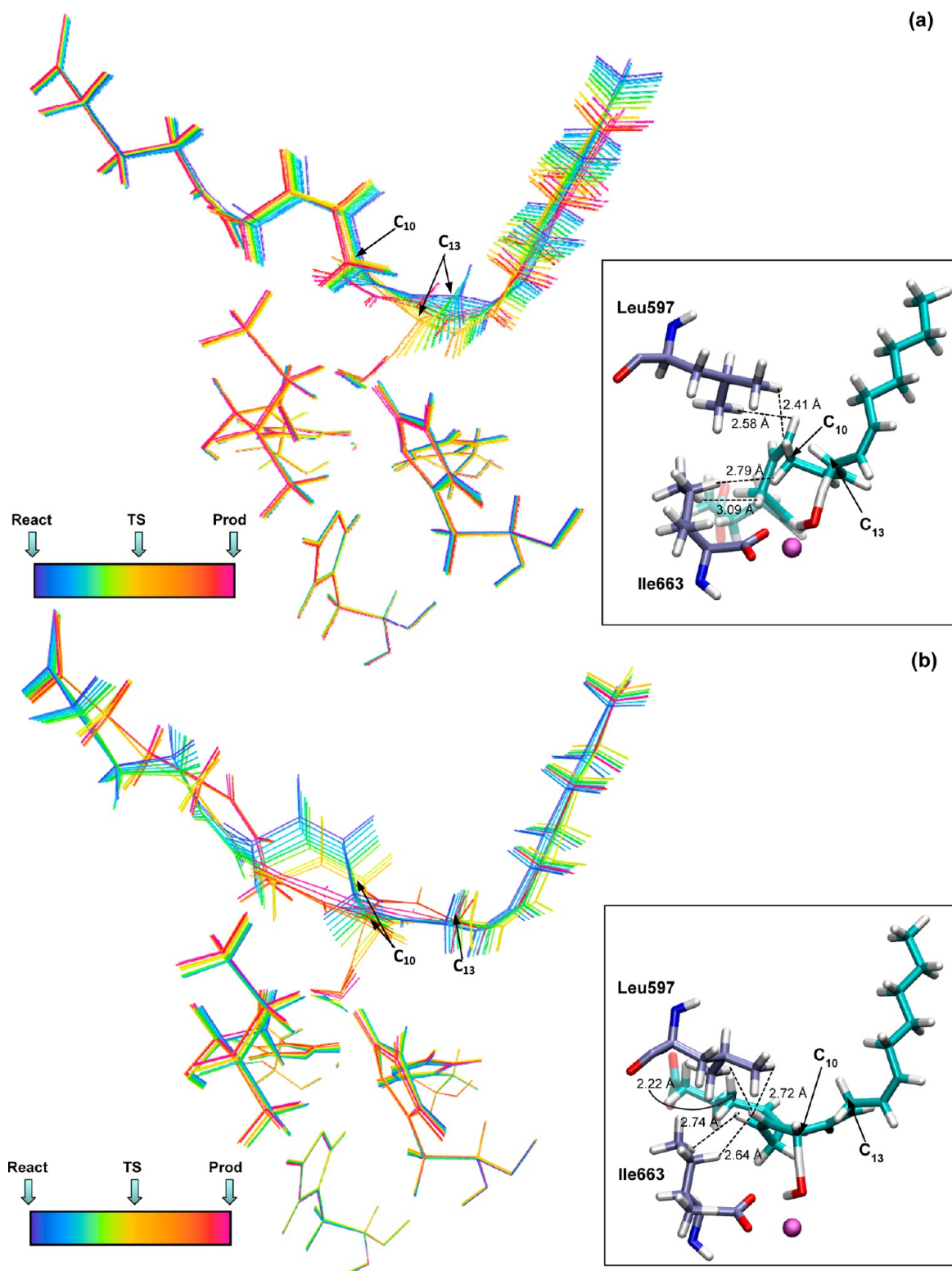
(a)

(b)

Figure 9. Representations of the structures along the reaction coordinates for H_{13} (a) and H_{10} (b) abstractions in structure XI. Color scale is used going from blue (reactants) to red (products). Boxes on the right show the closest distances from Ile663 and Leu597 to arachidonic acid in the transition state structures.

proaches planarity by conjugation in a π system consisting of five electrons (the unpaired electron originally at C_{13} and four π electrons of the two adjacent double bonds) delocalized over five carbon atoms (from C_{11} to C_{15}). Exactly the same happens for the H_{10} abstraction, now C_{10} being the atom tending to an sp^2 hybridization and C_8 to C_{12} being the carbon atoms forming

the planar AA-pentadienyl radical. The larger the geometrical change from an initially nonplanar structure to a planar pentadienyl and, especially, the greater steric hindrance to that motion, the higher the contribution to the potential energy barrier. In Figure 9 we have depicted the geometric evolution of the active site of structure XI along the hydrogen transfer, using

a scale of colors to visualize the progress from the reactant to the product. As for the H_{13} abstraction, the dihedral angles C_{11}–C_{12}–C_{13}–C_{14} and C_{12}–C_{13}–C_{14}–C_{15} at structure XI are 188.5° and 122.8°, respectively, whereas they become 165.7° and 176.7°, respectively, at the radical product. This change involves a small motion of AA (see Figure 9a), which does not practically affect the region of the C_8–C_9 double bond, that occurs in a region of the 15-rLO cavity without significant steric hindrance to the motion of AA. However, the dihedral angles C_8–C_9–C_{10}–C_{11} and C_9–C_{10}–C_{11}–C_{12} at structure XI are 105.7° and 109.9°, respectively, whereas they become −0.2° and 174.8°, respectively, at the radical product after the H_{10} abstraction. This change requires a broad motion of AA (see Figure 9b), fundamentally in the region of the C_8–C_9 double bond (from C_7 to C_{10}), where the side chains of Leu597 and Ile663 (especially the ethyl group attached to its β-carbon) significantly hinder the motion. The change of the dihedral angle C_8–C_9–C_{10}–C_{11} pushes the region of the C_8–C_9 double bond against Leu597 and Ile663. For instance, see in the inset of Figure 9b that the two hydrogen atoms, H_8 and H_9, in the C_8–C_9 double bond become very close to some hydrogen atoms of Leu597 and Ile663 (as close as 2.22 Å) at the H_{10} transition state structure. In contrast, the closest hydrogen atoms of AA, H_7, H_9, and H_{10}, to the hydrogen atoms of Leu597 and Ile663 practically do not move and keep somewhat farther along the H_{13} abstraction (see the transition state structure in the inset of Figure 9a). The compression along the hydrogen transfer of the C_8–C_9 double-bond region of AA against Leu597 and Ile663 when the H_{10} abstraction (but not for the H_{13} abstraction) occurs can be better seen in Figure 10, where the van der Waals surfaces of these critical regions are represented for the initial reactive structure XI, the H_{13} abstraction transition state structure, and the H_{10} abstraction transition state structure. It is worth noting that the van der Waals region around the C_8–C_9 double bond of AA at the H_{13} transition state structure (Figure 10b) matches the one at the reactant structure XI (Figure 10a), whereas the mobile van der Waals region around the C_8–C_9 double bond of AA at the H_{10} transition state structure (Figure 10c) evolves just up to the limits of the van der Waals regions of both Leu597 and Ile663.

The energy penalty of the interpenetration of two van der Waals regions is quite huge. To avoid that, the necessary evolution of the dihedral angles C_8–C_9–C_{10}–C_{11} and C_9–C_{10}–C_{11}–C_{12} requires the intense motion of the AA head, as seen in Figure 9b. This is the cause of the higher value of the $\Delta E^{\ddagger}_{(MM,QM)}$ term (see Table 3) for the H_{10} abstraction in comparison to the H_{13} abstraction in structure XI. An analysis of the different energy terms clarifies this point. The van der Waals contributions of Leu597 to the potential energy barriers for the H_{13} and H_{10} abstractions are 0.20 and 0.17 kcal/mol, respectively. Likewise, the respective values for Ile663 are 0.19 and −0.05 kcal/mol. All of those values turn out to be very small, therefore corroborating that the van der Waals regions in the case of the H_{10} abstraction stop just before collision. This fact forces the distortion of the AA head to allow the change of the dihedral angles C_8–C_9–C_{10}–C_{11} and C_9–C_{10}–C_{11}–C_{12} to occur. This distortion pays an energy penalty, but lower than the one that would be associated with the interpenetration of the van der Waals surfaces. Therefore, the motion of the C_1–C_6 head of AA implies an electrostatic contribution of 7.5 kcal/mol to the H_{10} potential energy barrier, but just of −0.75 kcal/mol for the H_{13} case. That H_{10} electrostatic contribution is due in part to the weakening of the Arg403−carboxylate of AA
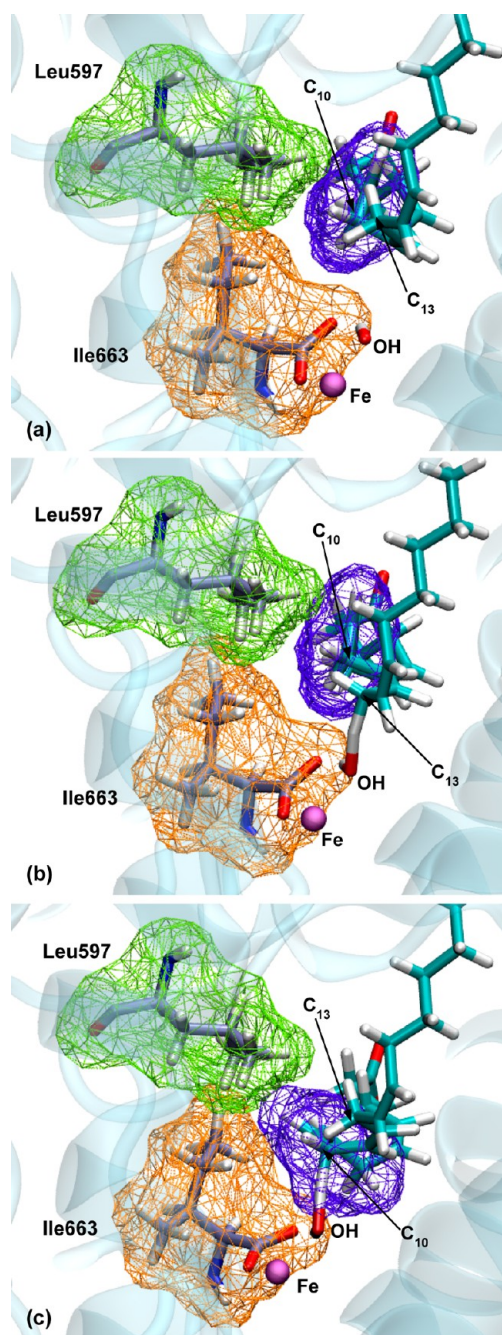

Figure 10. Representation of the van der Waals surfaces of Ile663 (orange), Leu597 (green), and all atoms from C_7 to C_{10} of AA (blue). Atoms of AA, OH, and Ile663 are highlighted by using the licorice drawing method. These pictures correspond to structure XI: (a) reactant; (b) TS of H_{13} abstraction; (c) TS of H_{10} abstraction.

interaction (as can be seen in Figures S2−S5), which costs 2.3 kcal/mol, in contrast with the case of H_{13} (−0.14 kcal/mol). In addition, the contribution to the energy barrier of the deformation of the C_1–C_6 bond angles is 2.6 kcal/mol for H_{10}, but only −0.43 kcal/mol for H_{13}. To summarize, we conclude that the subtle steric hindrance by Leu597 and Ile663 is mainly responsible for the difference between the H_{13}/H_{10} potential energy barriers and reaction energies in structure XI. This steric hindrance, as usual, does not produce an increase of the energy associated with the van der Waals terms, but provokes additional motions in other parts of the system, just

to circumvent the huge penalty that should be paid for the interpenetration of two van der Waals regions.

In general, the H_{10} abstraction is disfavored in comparison with the H_{13} abstraction due to the steric hindrance by Leu597 or Ile663 or both at the same time. In some structures even Ile173 contributes to that hindrance. This gives rise to somewhat higher potential energy barriers for the H_{10} abstraction than for the H_{13} abstraction, so explaining the strict regiospecificity of the first step of the hydroperoxidation of AA by 15-rLO and 15-hLO, despite the fact that both hydrogen abstractions from C_{13} and from C_{10} would seem feasible. As for Ile663, in all nine structures selected as suitable for the H_{13} abstraction the ethyl group bonded to the β-carbon of Ile663 is the one that faces the C_8–C_9 double-bond region of AA. Conversely, only structures selected for the H_{10} abstraction where the shorter methyl group of that β-carbon (structures XII–XVI) is the one oriented toward the C_8–C_9 double-bond region of AA give rise to the H_{10} abstraction with an energy barrier of <26 kcal/mol. The hindrance by the methyl group is indeed lower than by the ethyl group, but the effect is still significant.

To compare with the experimental results, we should calculate something like an average potential energy barrier. We could run a long classical MD trajectory and aleatorily select a huge number of snapshots without any predefined criterium of choice. Then we could calculate for each of them the potential energy barrier corresponding to the hydrogen abstraction. Assuming that each snapshot reacts with a local rate constant that fulfills the conventional transition state theory and that the free energy and the potential energy barriers have similar values,[48] the average potential energy barrier that would correspond to the overall rate constant could be obtained using the equation[49,50]

$$\Delta E^{\ddagger}_{AV} = -RT \ln \left\{ \frac{1}{n} \sum_{i=1}^{n} \exp\left(\frac{-\Delta E^{\ddagger}_i}{RT} \right) \right\} \tag{3}$$

where R is the gas constant, T is the temperature, $\Delta E^{\ddagger}_i$ is the potential energy barrier for each snapshot, and n is the number of snapshots generated. However, the aleatory choice of a very large number of snapshots without any selection criterium and its use in eq 3 are nowadays out of our computational capabilities. Instead, we have used eq 3 along with the results given in Table 3: the potential energy barriers corresponding to structures I–XI for the H_{13} abstraction and the ones arising from structures X–XVII for the H_{10} abstraction. Therefore, the obtained average potential energy barriers are 19.6 kcal/mol for the H_{13} abstraction and 23.6 kcal/mol for the H_{10} abstraction at $T = 300$ K. This difference of 4.0 kcal/mol agrees well with the value of 2.1 kcal/mol derived from the experimental C_{13}:C_{10} ratio of 97:3 for 15-rLO, assuming kinetic control for the regiospecificity and employing conventional transition state theory as specified above. On the other hand, we have already mentioned above that there appear along the MD simulations significantly more structures with the H_{10} close to the Fe(III)–OH^- cofactor than with the H_{13}. This fact could indicate that the consideration of a huge number of MD snapshots as starting points to generate many more reaction channels could lower that theoretical difference of 4 kcal/mol, becoming closer to the experimental value of 2.1 kcal/mol.

The accuracy of the calculated potential energy barriers has been assessed by means of single-point energy calculations to examine the sensitivity of the results to the choice of functional

and basis set. The 40 new potential energy barriers for H_{13} and H_{10} abstractions are given in Table S2 of the Supporting Information. It can be observed that only small changes of the potential energy values are obtained by using the Ahlrichs-vtz triple-ζ basis set[51] and the TPSSH functional.[52] Thus, the difference of the average potential energy barriers (calculated according to eq 3) for H_{13} versus H_{10} abstraction is 4.5 kcal/mol with the Ahlrichs-vtz basis set and 3.9 kcal/mol with the TPSSH functional, in good agreement with the double-ζ B3LYP result given above. As the inclusion of dispersion energy in DFT/MM calculations in enzyme-catalyzed reactions has been shown to be important, we have also recomputed the 20 potential energy barriers by means of single-point energy calculations using the B3LYP-D2 functional with Grimme-type corrections[53] (see Table S2). The inclusion of dispersion effects somewhat decreases the potential energy barriers of H_{13} and H_{10} abstractions but without a significant change in their relative barriers, the dispersion-corrected average potential energy difference being 4.7 kcal/mol. In Table S3 we have also included the zero-point energy (ZPE) corrected B3LYP/ [LANDZ2D(Fe), 6-31G(d) (rest)] barriers for all of the H_{13} and H_{10} abstractions. It can be observed that the inclusion of the ZPE lowers the H-abstraction barriers, but it does not modify the average energy difference of 4.0 kcal/mol favoring H_{13} abstraction versus H_{10} abstraction.

At this point, we would like to make some final remarks concerning the methodology employed in this study. On the one hand, in a previous paper[54] for the hydrogen abstraction from linoleic acid catalyzed by soybean lipoxygenase-1, that is, a system quite similar to our current system, we showed that the QM/MM potential energy profile and the potential of mean force (PMF) were quite similar, so indicating that the thermal and entropic contributions to the free energy were small. We think that the same thing would happen in the current case, and for this reason we have not included those contributions here. As for quantum tunneling, it would be expected to increase H_{13} and H_{10} abstraction rate constants. However, the distributions of reaction path lengths are quite similar for H_{13} and H_{10} abstractions. Then, despite the somewhat higher potential energy barriers for H_{10} than for H_{13} abstraction, it is expected that quantum tunneling will not significantly modify the H_{13}/H_{10} rate constants ratio. Finally, we want to emphasize that calculations based on transition state theory work well for lipoxygenases, leading to reliable results that satisfactorily compare with experiments.

4. CONCLUSIONS

Many enzymes are able to activate C–H bonds in complex molecules containing several of them with an exquisite regiospecificity, a difficult task to achieve by conventional chemical methods. In this paper we have employed quantum mechanics/molecular mechanics methods to study the mechanism of the hydrogen abstraction reaction from arachidonic acid (AA) catalyzed by 15-rLO, an enzyme that has approximately 80% sequence identity with 15-hLO. These enzymes exhibit a very high regiospecificity, in such a way that most of the products arise from the initial hydrogen abstraction from the carbon C_{13} of AA.[17–19] It has been assumed that this regiospecificity of the different mammalian lipoxygenase isoenzymes is due to the depth and width of the substrate binding pocket and the head/tail orientation of the incoming AA, in such a way that each lipoxygenase enzyme would abstract a hydrogen atom from essentially a unique position,

the only one that is able to be close to the oxygen acceptor atom of the Fe(III)−OH⁻ cofactor. However, unexpected experimental results for 15-hLO have suggested that the hydrogen abstractions from two structurally different positions (C_{13} and C_{10}) follow a comparable mechanism[18−20] with similar transition state structures, which does not seem very compatible with the known exquisite regiospecificity of this enzyme.

Our results show that there exists a wide dispersion of geometries of the AA:15-rLO Michaelis complexes in a good disposition to transfer one of the hydrogen atoms to the acceptor oxygen atom. Some of these reactive structures are ready to transfer a hydrogen atom (H_{13}) attached to C_{13}, some are prepared to transfer a hydrogen atom (H_{10}) attached to C_{10}, and some others are even set to transfer any of both. Hence, in principle, 15-rLO could catalyze not only the abstraction of H_{13} but also the abstraction of H_{10}. Very interestingly, after having studied 11 hydrogen transfers of H_{13}, starting from the corresponding 11 reactive structures we have selected, we have found that the geometries around the shifting H_{13} of the 11 transition state structures are very similar. However, we have obtained a wide range of potential energy barriers, which can be attributed to the initial geometric dispersion of the reactive minima. Something similar occurs for the nine H_{10} hydrogen transfers studied: all of the transition states are similar, but with different potential energy barriers, which tend to be somewhat higher than for the H_{13} abstractions. Even more, when comparing the H_{13} and H_{10} abstractions, we see that the reaction mechanisms for both are identical (proton-coupled electron transfer processes), with transition state structures that match their geometries around the shifting hydrogen. This confirms the suggestion by Holman and co-workers[18−20] about the similarity of the mechanisms and transition states for both abstractions.

The average potential energy barriers we have obtained are 19.6 kcal/mol for the H_{13} abstraction and 23.6 kcal/mol for the H_{10} abstraction. This difference of 4.0 kcal/mol agrees well with the value of 2.1 kcal/mol derived from the experimental C_{13}:C_{10} ratio of 97:3 for 15-rLO. Steric hindrance by residues Leu597 and Ile663 turn out to be mainly responsible for that difference. As for the second residue, the catalytic iron is coordinated by the main-chain carboxylate of the C terminal Ile663, which contributes to determine the electronic density on this iron atom and so regulates its redox potential. In addition, that carboxylate forms a hydrogen bond with the hydrogen atom of the OH⁻ group of the Fe(III)−OH⁻ cofactor, so helping the right positioning of that OH⁻. However, any of the amino acids with aliphatic side-chain groups (Gly, Ala, ...) could have been adequate to play exactly the same role. Why then has nature chosen just the bulkiest of all them? This is because the large side chains of Ile663 and Leu597 significantly hinder the geometric evolution that AA needs to experience during the H_{10} abstraction but have no role when H_{13} is transferred. Therefore, we conclude that, despite the fact that AA can perfectly accommodate both H_{13} and H_{10} to be transferred, the subtle steric hindrance by Leu597 and Ile663 of 15-rLO turns out to be the main cause for the difference between the H_{13}/H_{10} potential energy barriers and, as a consequence, for the strict regiospecificity exhibited by the enzyme 15-lipoxygenase-1. It has to be emphasized that these residues are conserved in the mammalian lipoxygenase isoenzymes, where they are probably also responsible for discerning between the two hydrogen atoms of AA that can be positioned to be transferred. The crucial physiological role of all these enzymes would not be possible without the regiospecificity induced by such a subtle effect. We hope that this finding will be useful to understand how other enzymes work and to encourage new experiments in this field. Moreover, our results can be useful to design by protein engineering efficient biocatalysts for the selective activation of C−H bonds.

■ ASSOCIATED CONTENT

ⓢ Supporting Information

The following file is available free of charge on the ACS Publications website at DOI: 10.1021/cs5006103.

> Number of active and total atoms in the studied structures, H-abstraction potential energy barriers at different levels of theory, zero-point energy corrected H-abstraction energy barriers, correlations of potential energy barriers and geometrical parameters, representation of AA carboxylate end−Arg403 interaction at the H-abstraction reactant and transition states (PDF).

■ AUTHOR INFORMATION

Corresponding Author

*(A.G.-L.) E-mail: Angels.Gonzalez@uab.cat.

Notes

The authors declare no competing financial interest.

■ ACKNOWLEDGMENTS

■ REFERENCES

(1) Catalano, A.; Procopio, A. *Histol. Histopath.* **2005**, *20*, 969−975 ISSN 1699-5848.

(2) Dobrian, A. D.; Lieb, D. C.; Cole, B. K.; Taylor-Fishwick, D. A.; Chakrabarti, S. K.; Nadler, J. L. *Prog. Lipid Res.* **2011**, *50*, 115−131.

(3) Haeggstrom, J. Z.; Funk, C. D. *Chem. Rev.* **2011**, *111*, 5866−5898.

(4) Joo, Y. C.; Oh, D. K. *Biotechnol. Adv.* **2012**, *30*, 1524−1532.

(5) Coffa, G.; Brash, A. R. *Proc. Natl. Acad. Sci. U. S. A.* **2004**, *101*, 15579−15584.

(6) Ivanov, I.; Heydeck, D.; Hofheinz, K.; Roffeis, J.; O'Donnell, V. B.; Kühn, H.; Walther, M. *Arch. Biochem. Biophys.* **2010**, *503*, 161−174.

(7) Schneider, C.; Pratt, D. A.; Porter, N. A.; Brash, A. R. *Chem. Biol.* **2007**, *14*, 473−488.

(8) Schwarz, K.; Walther, M.; Anton, M.; Gerth, C.; Feussner, I.; Kühn, H. *J. Biol. Chem.* **2001**, *276*, 773−779.

(9) Vogel, R.; Jansen, C.; Roffeis, J.; Reddanna, P.; Forsell, P.; Claesson, H. E.; Kühn, H.; Walther, M. *J. Biol. Chem.* **2010**, *285*, 5369−5376.

(10) Suardíaz, R.; Masgrau, L.; González-Lafont, À.; Lluch, J. M. *FEBS J.* **2013**, *280*, 94−94.

(11) Suardíaz, R.; Masgrau, L.; Lluch, J. M.; González-Lafont, À. *J. Phys. Chem. B* **2013**, *117*, 3747−3754.

(12) Suardíaz, R.; Masgrau, L.; Lluch, J. M.; González-Lafont, À. *ChemPhysChem* **2013**, *14*, 3777−3787.

(13) Suardíaz, R.; Masgrau, L.; Lluch, J. M.; González-Lafont, À. *ChemPhysChem* **2014**, *15*, 2303−2310.

(14) Choi, J.; Chon, J. K.; Kim, S.; Shin, W. *Proteins* **2008**, *70*, 1023−1032.

(15) Gillmor, S. A.; Villasenor, A.; Fletterick, R.; Sigal, E.; Browner, M. F. *Nat. Struct. Biol.* **1997**, *4*, 1003−1009.

(16) Rai, G.; Kenyon, V.; Jadhav, A.; Schultz, L.; Armstrong, M.; Jameson, J. B.; Hoobler, E.; Leister, W.; Simeonov, A.; Holman, T. R.; Maloney, D. J. *J. Med. Chem.* **2010**, *53*, 7392−7404.

(17) Gan, Q. F.; Browner, M. F.; Sloane, D. L.; Sigal, E. *J. Biol. Chem.* **1996**, *271*, 25412−25418.

(18) Jacquot, C.; Wecksler, A. T.; McGinley, C. M.; Segraves, E. N.; Holman, T. R.; van der Donk, W. A. *Biochemistry* **2008**, *47*, 7295−7303.

(19) Borngraber, S.; Browner, M.; Gillmor, S.; Gerth, C.; Anton, M.; Fletterick, R.; Kühn, H. *J. Biol. Chem.* **1999**, *274*, 37345−37350.

(20) Wecksler, A. T.; Jacquot, C.; van der Donk, W. A.; Holman, T. R. *Biochemistry* **2009**, *48*, 6259−6267.

(21) Toledo, L.; Masgrau, L.; Marechal, J. D.; Lluch, J. M.; González-Lafont, À. *J. Phys. Chem. B* **2010**, *114*, 7037−7046.

(22) Costas, M.; Mehn, M. P.; Jensen, M. P.; Que, L. *Chem. Rev.* **2004**, *104*, 939−986.

(23) Ferreira, E. M. *Nat. Chem.* **2014**, *6*, 94−96.

(24) Groves, J. T. *Nat. Chem.* **2014**, *6*, 89−91.

(25) Negretti, S.; Narayan, A. R. H.; Chiou, K. C.; Kells, P. M.; Stachowski, J. L.; Hansen, D. A.; Podust, L. M.; Montgomery, J.; Sherman, D. H. *J. Am. Chem. Soc.* **2014**, *136*, 4901−4904.

(26) Sherwood, P.; de Vries, A. H.; Guest, M. F.; Schreckenbach, G.; Catlow, C. R. A.; French, S. A.; Sokol, A. A.; Bromley, S. T.; Thiel, W.; Turner, A. J.; Billeter, S.; Terstegen, F.; Thiel, S.; Kendrick, J.; Rogers, S. C.; Casci, J.; Watson, M.; King, F.; Karlsen, E.; Sjovoll, M.; Fahmi, A.; Schafer, A.; Lennartz, C. *Theochem-J. Mol. Struct.* **2003**, *632*, 1−28.

(27) Ahlrichs, R.; Bar, M.; Haser, M.; Horn, H.; Kolmel, C. *Chem. Phys. Lett.* **1989**, *162*, 165−169.

(28) Smith, W.; Forester, T. R. *J. Mol. Graph.* **1996**, *14*, 136−141.

(29) MacKerell, A. D.; Bashford, D.; Bellott; Dunbrack, R. L.; Evanseck, J. D.; Field, M. J.; Fischer, S.; Gao, J.; Guo, H.; Ha, S.; Joseph-McCarthy, D.; Kuchnir, L.; Kuczera, K.; Lau, F. T. K.; Mattos, C.; Michnick, S.; Ngo, T.; Nguyen, D. T.; Prodhom, B.; Reiher, W. E.; Roux, B.; Schlenkrich, M.; Smith, J. C.; Stote, R.; Straub, J.; Watanabe, M.; Wiorkiewicz-Kuczera, J.; Yin, D.; Karplus, M. *J. Phys. Chem. B* **1998**, *102*, 3586−3616.

(30) Mackerell, A. D.; Feig, M.; Brooks, C. L. *J. Comput. Chem.* **2004**, *25*, 1400−1415.

(31) Feller, S. E.; Gawrisch, K.; MacKerell, A. D. *J. Am. Chem. Soc.* **2001**, *124*, 318−326.

(32) Feller, S. E.; MacKerell, A. D. *J. Phys. Chem. B* **2000**, *104*, 7510−7515.

(33) Bakowies, D.; Thiel, W. *J. Phys. Chem.* **1996**, *100*, 10580−10594.

(34) de Vries, A. H.; Sherwood, P.; Collins, S. J.; Rigby, A. M.; Rigutto, M.; Kramer, G. J. *J. Phys. Chem. B* **1999**, *103*, 6133−6141.

(35) Liu, D. C.; Nocedal, J. *Math. Program.* **1989**, *45*, 503−528.

(36) Nocedal, J. *Math. Comput.* **1980**, *35*, 773−782.

(37) Baker, J. *J. Comput. Chem.* **1986**, *7*, 385−395.

(38) Banerjee, A.; Adams, N.; Simons, J.; Shepard, R. *J. Phys. Chem.* **1985**, *89*, 52−57.

(39) Billeter, S. R.; Turner, A. J.; Thiel, W. *PCCP Phys. Chem. Chem. Phys.* **2000**, *2*, 2177−2186.

(40) Reed, A. E.; Weinstock, R. B.; Weinhold, F. *J. Chem. Phys.* **1985**, *83*, 735−746.

(41) Humphrey, W.; Dalke, A.; Schulten, K. *Journal of Molecular Graphics & Modelling* **1996**, *14*, 33−38.

(42) Harihara, Pc; Pople, J. A. *Theor. Chim. Acta* **1973**, *28*, 213−222.

(43) Hay, P. J.; Wadt, W. R. *J. Chem. Phys.* **1985**, *82*, 270−283.

(44) Hatcher, E.; Soudackov, A. V.; Hammes-Schiffer, S. *J. Am. Chem. Soc.* **2004**, *126*, 5763−5775.

(45) Hatcher, E.; Soudackov, A. V.; Hammes-Schiffer, S. *J. Am. Chem. Soc.* **2007**, *129*, 187−196.

(46) Huynh, M. H. V.; Meyer, T. J. *Chem. Rev.* **2007**, *107*, 5004−5064.

(47) Weinberg, D. R.; Gagliardi, C. J.; Hull, J. F.; Murphy, C. F.; Kent, C. A.; Westlake, B. C.; Paul, A.; Ess, D. H.; McCafferty, D. G.; Meyer, T. J. *Chem. Rev.* **2012**, *112*, 4016−4093.

(48) Claeyssens, F.; Harvey, J. N.; Manby, F. R.; Mata, R. A.; Mulholland, A. J.; Ranaghan, K. E.; Schutz, M.; Thiel, S.; Thiel, W.; Werner, H.-J. *Angew. Chem., Int. Ed.* **2006**, *45*, 6856−6859.

(49) Lonsdale, R.; Harvey, J. N.; Mulholland, A. J. *J. Phys. Chem. B* **2010**, *114*, 1156−1162.

(50) Lonsdale, R.; Houghton, K. T.; Zurek, J.; Bathelt, C. M.; Foloppe, N.; de Groot, M. J.; Harvey, J. N.; Mulholland, A. J. *J. Am. Chem. Soc.* **2013**, *135*, 8001−8015.

(51) Schafer, A.; Horn, H.; Ahlrichs, R. *J. Chem. Phys.* **1992**, *97*, 2571−2577.

(52) Tao, J.; Perdew, J. P.; Staroverov, V. N.; Scuseria, G. E. *Phys. Rev. Lett.* **2003**, *91*, 146401−146404.

(53) Grimme, S. *J. Comput. Chem.* **2006**, *27*, 1787−1799.

(54) Tejero, I.; Garcia-Viloca, M.; González-Lafont, À.; Lluch, J. M.; York, D. M. *J. Phys. Chem. B* **2006**, *110*, 24708−24719.